Journal of Geodesy (2021) 95:124
https://doi.org/10.1007/s00190-021-01577-7

ORIGINAL ARTICLE

Midlatitude climatology of the ionospheric equivalent slab thickness over two solar cycles

Alessio Pignalberi[1] · Bruno Nava[2] · Marco Pietrella[1] · Claudio Cesaroni[1] · Michael Pezzopane[1]

Received: 20 December 2020 / Accepted: 3 October 2021

Abstract
The main climatological features of the ionospheric equivalent slab thickness (τ) for the Northern hemisphere midlatitudes are analyzed. F2-layer peak electron density values recorded at three midlatitude ionospheric stations (Chilton 51.5° N, 0.6° W, U.K.; Roquetes 40.8° N, 0.5° E, Spain; Wallops Island 37.9° N, 75.5° W, USA) and vertical total electron content values from colocated ground-based Global Navigation Satellite System receivers are used to calculate a dataset of τ values for the last two solar cycles, considering only magnetically quiet periods. Results are presented both as grids of binned medians and as boxplots as a function of local time and month of the year, for different solar activity levels. Corresponding trends are first compared to those output by the midlatitude empirical model developed by Fox et al. (Radio Sci 26:429–438, 1991) and then discussed in the light of what is known so far. From this investigation, the strong need to implement an improved empirical model of τ has emerged. Both Space Weather and Space Geodesy applications might benefit from such model. Therefore, both the dataset and the methodology described in the paper represent a first fundamental step aimed at implementing an empirical climatological model of the ionospheric equivalent slab thickness. The study highlighted also that at midlatitudes τ shows the following main patterns: daytime values considerably smaller than nighttime ones (except in summer); well-defined maxima at solar terminator hours; a greater dispersion during nighttime and solar terminator hours; no clear and evident solar activity dependence.

Keywords Ionospheric equivalent slab thickness · Climatological model · Midlatitude ionosphere · Solar activity

1 Introduction

The ionospheric equivalent slab thickness (τ) is defined as the ratio of the vertical total electron content (vTEC) to the F2-layer peak electron density (*Nm*F2) (Titheridge 1973; Davies 1990); so, τ is a characteristic parameter of the electron density profile representing the equivalent thickness of an ionosphere of uniform electron density equal to *Nm*F2. Thick electron density profiles are characterized by higher τ values, while lower τ values are associated with sharper profiles. For a given *Nm*F2, the shape of the ionospheric electron density profile critically depends on the different contribution that the bottomside and the topside parts give to vTEC (e.g., Jayachandran et al. 2004; Pezzopane et al. 2019).

Besides the profile shape, in the past, many authors linked τ to other physical variables and ionosphere properties. For example, Wright (1960) and Titheridge (1973), in the simplifying working hypothesis of an α-Chapman shape for the F2 layer, related τ to the neutral scale height H_n of the atmosphere according to the relation $\tau = 4.13\ H_n$. However, it should be noted that this relation is valid for an α-Chapman function that represents the F2 layer of the ionosphere only under very strict assumptions, which are not fully met in the case of the real ionosphere. In fact, the vertical distribution of the ionospheric plasma is driven by the plasma scale height H_p that, in turn, depends on the plasma temperature, ion composition, and other physical quantities (e.g., Pignalberi et al. 2018, 2020a,b). The search for a link between τ and neutral or plasma scale heights, as well as a dependence of τ on the plasma and neutral temperatures, is a very hot topic as testified by investigations of different authors, e.g., Stankov and Jakowski (2006), Jakowski et al. (2017).

✉ Alessio Pignalberi
alessio.pignalberi@ingv.it

[1] Istituto Nazionale Di Geofisica E Vulcanologia, Via di Vigna Murata 605, 00143 Rome, Italy

[2] The Abdus Salam International Centre for Theoretical Physics, Strada Costiera 11, 34151 Trieste, Italy

Published online: 23 October 2021

The τ behavior is rather complex because it is affected by the simultaneous variability of both the bottomside and the topside ionosphere and also by important plasmaspheric processes. The climatological and non-climatological features of τ were studied by many authors, and to this regard, a very wide literature exists. The diurnal, seasonal, geographic, solar activity, and magnetic activity variations have been shown to be of great relevance for the τ description. The corresponding climatological behavior has been extensively studied during maximum and minimum solar phases, for midlatitudes stations located in the Northern hemisphere (e.g., Fox et al. 1991; Jayachandran et al. 2004; Stankov and Warnant 2009; Chuo et al. 2010; Haralambous 2011; Mosert et al. 2013; Jakowski et al. 2017), and in the Southern hemisphere (Goodwin et al. 1995; Breed et al. 1997).

These studies showed that, depending on the considered station, τ presents significant diurnal, seasonal, solar and magnetic activity variations. The main outcomes from the existing literature are as follows:

(a) The presence of a pre-sunrise peak in winter, summer, and equinoctial months for both low solar activity (Davies and Liu 1991; Jayachandran et al. 2004; Stankov and Warnant 2009; Haralambous 2011; Mosert et al. 2013) and high solar activity (Minakoshi and Nishimuta 1994; Stankov and Warnant 2009; Chuo et al. 2010);
(b) Independently of the solar activity, daytime values are smaller than nighttime ones except for summer (Davies and Liu 1991; Jayachandran et al. 2004; Stankov and Warnant 2009; Chuo et al. 2010; Haralambous 2011; Mosert et al. 2013);
(c) The presence of a post-sunset peak in winter for low solar activity (Jayachandran et al. 2004; Stankov and Warnant 2009; Haralambous 2011; Mosert et al. 2013; Huang and Yuan 2015), and in summer for both medium solar activity (Jin et al. 2007) and high solar activity (Stankov and Warnant 2009).

The dependence of the long-term trend of τ on solar cycle variations was also widely studied at midlatitudes (e.g., Bhonsle et al. 1965; Tyagi and Somayajulu 1966; Dabas et al. 1984; Davies and Liu 1991; Jayachandran et al. 2004; Jakowski et al. 2017). In particular, Davies and Liu (1991) found a linearly increasing trend of τ with the smoothed solar radio flux at 10.7 cm (F10.7) for all seasons at noontime. Also, Jayachandran et al. (2004) found a linear increase in τ with F10.7 in summer and equinox months for high solar activity, while they observed a decreasing trend in winter for low solar activity.

With regard to the τ calculation, the different methodologies that can be applied to retrieve vTEC data play a crucial role in the achievement of reliable results (Pignalberi et al. 2021); conversely, *Nm*F2 data are always obtained by scaling the critical frequency *fo*F2 of the ionospheric F2-layer associated with the ordinary mode of propagation from ionograms recorded by ionosondes and then by applying the formula $NmF2 = (1.24 \times 10^{10}) \cdot foF2^2$, where *Nm*F2 is expressed in (el/m^3) and *fo*F2 in (MHz) (Davies 1990). Also, *fo*F2 can be affected by the different methods used for the automatic ionograms scaling or by a human bias introduced by different operators (Pezzopane and Scotto 2005, 2007).

Studies on τ performed between 60's and 90's are based on vTEC values from Faraday rotation or Doppler frequency shift of satellites radio signals (Titheridge 1972). By using these techniques, some limitations are introduced. For example, the calculation of vTEC from Faraday rotation induced on geostationary satellite signals needs the assumption of a constant magnetic factor along the ray path. Titheridge (1972) stated that this is reasonably true by neglecting the effects of the electron density above 2000 km. As a consequence, Faraday rotation measurements from geostationary satellite signals can give the vTEC only up to 2000 km (Titheridge 1972; Davies 1990). Recently, Global Navigation Satellite System (GNSS) dual-frequency satellites became available for vTEC calculation. Differently from Faraday rotation or Doppler frequency shift methodologies, vTEC measurements from GNSS satellites include the contribution of the plasmasphere. As a matter of fact, some differences, both in the vTEC absolute value and in its climatological behavior, might arise and have to be taken into account when making comparison studies with the less recent literature. As an example of that, we will show a comparison between binned measured median τ values, at Wallops Island station, and those calculated by the Fox et al. (1991) model, which is an empirical model describing the main climatological trends of τ at midlatitudes.

A reliable knowledge of the τ behavior is of primary importance for several data-assimilation methods for the now-casting of vTEC or *Nm*F2, when one of the two parameters is available (Krankowski et al. 2007; Gerzen et al. 2013; Froń et al. 2020). A weakness in the representation of τ can lead to *fo*F2 retrieval errors when vTEC data are ingested into NeQuick 2, as indicated by Nava et al. (2011). The need of a reliable global scale modeling of τ is testified by the empirical climatological model recently proposed by Jakowski and Hoque (2021), which is the only global model available so far. They modeled τ on the basis of a dataset of *Nm*F2 values derived by radio occultation observations from different satellite missions and vTEC values from maps based on ground-based GNSS data. Their model reproduces the main τ climatological variations and anomalies on a global scale via nonlinear least square regressions based on 12 coefficients, thus providing a smooth representation of the median τ behavior.

Table 1 List of the considered ionosonde stations along with the corresponding geographic coordinates, the Quasi-Dipole magnetic latitude (Laundal and Richmond 2017), and the corresponding data availability

Ionosonde (country)	Geographic latitude	Geographic longitude	Quasi-Dipole latitude	Years dataset
Chilton (U.K.)	51.5° N	0.6° W	47.8° N	1997–2019
Roquetes (Spain)	40.8° N	0.5° E	34.9° N	1997–2019
Wallops Island (USA)	37.9° N	75.5° W	47.7° N	1999–2019

Table 2 List of considered ground-based GNSS receiver stations, colocated with ionosonde stations

GNSS receiver location (CODE)	Colocated ionosonde (distance in km)	Geographic latitude	Geographic longitude	Years dataset
Hailsham (HERS)	Chilton (96)	50.9° N	0.3° W	1997–2019
Roquetes (EBRE)	Roquetes (0)	40.8° N	0.5° E	1997–2019
Cambridge (HNPT)	Wallops Island (94)	38.6° N	76.1° W	1999–2019

Corresponding distances (in km) between GNSS and ionosonde stations, geographic coordinates and the corresponding data availability, are also shown

This paper analyzes the main climatological features of τ at midlatitudes. *Nm*F2 data from three midlatitude stations (Chilton 51.5° N, 0.6° W, U.K.; Roquetes 40.8° N, 0.5° E, Spain; Wallops Island 37.9° N, 75.5° W, USA) and vTEC values from colocated ground-based GNSS receivers have been used to calculate τ time series over a very long time window spanning the last two solar cycles (from 1997 to 2019). As far as we know, this is the longest dataset ever used for a climatological analysis of τ. Through this dataset, the diurnal, seasonal, and solar activity trends shown by τ at three midlatitude stations for magnetically quiet conditions are described and compared to the literature. Moreover, a comparison between measured and modeled τ values reveals that the Fox et al. (1991) model cannot properly describe all the climatological features of τ. This fact highlights the need of implementing an improved empirical model of τ based on vTEC values from GNSS. The dataset and the methodology here described are then very valuable for a future implementation of an empirical climatological model of the ionospheric equivalent slab thickness of which both Space Weather and Space Geodesy applications might benefit.

Section 2 describes the *Nm*F2 and vTEC data selection and filtering, along with the τ calculation and corresponding binning procedures. In the same section, the Fox et al. (1991) τ model is introduced. Section 3 compares for Wallops Island the binned measured median τ values with the corresponding ones given by the Fox et al. (1991) model. Moreover, it describes also the results for the two European stations of Chilton and Roquetes, highlighting and discussing the main differences and similarities characterizing the considered stations. Finally, Sect. 4 outlines the main findings and possible further extensions of the work.

2 Data and method

2.1 vTEC and *Nm*F2 datasets

The bulk of the *Nm*F2 dataset used in this study consists of data measured during the last two solar cycles (from the beginning of 1997 to the end of 2019) by the midlatitude ionosonde stations of Chilton, Roquetes, and Wallops Island (Table 1). *Nm*F2 values were downloaded from the Digital Ionogram DataBASE (Reinisch and Galkin 2011) through the SAO Explorer software developed at the University of Massachusetts, Lowell (http://ulcar.uml.edu/SAO-X/SAO-X.html). For all the three stations, ionograms were recorded by DPS Digisondes (Bibl and Reinisch 1978) and autoscaled by the Automatic Real-Time Ionogram Scaler with True height analysis (ARTIST) software (Galkin and Reinisch 2008). ARTIST flags the reliability of autoscaled parameters through the Confidence Score (C-Score) parameter (http://www.ursi.org/files/CommissionWebsites/INAG/web-73/confidence_score.pdf). Only ionograms with C-Score ≥ 75 were selected for this study. However, when manually scaled ionograms were available, they were used instead of autoscaled ones. *Nm*F2 time series have a fifteen-minute sampling interval according to the sounding repetition rate of the digisondes at minutes 0, 15, 30, and 45 of each Universal Time (UT) hour. The ionospheric observatory of Chilton, for most of the time, had a ten minutes sampling; in those cases, values recorded at minutes 10 and 40 are considered instead of 15 and 45.

To calculate τ values, we selected GNSS ground-based receivers of the International GNSS Service (IGS, http://www.igs.org/) network as near as possible to the ionosonde stations of Table 1 and with a long enough time series of

measurements. Table 2 lists the selected GNSS receivers: HERS located 96 km away from Chilton, EBRE colocated with Roquetes, and HNPT located 94 km away from Wallops Island. Daily Receiver INdependent EXchange (RINEX) formatted files containing L1 and L2 code and carrier phase data at a 30 s sampling time were downloaded from NASA's GNSS FTP repository (https://cddis.nasa.gov/Data_and_Derived_Products/CDDIS_Archive_Access.html). The equivalent vTEC values at the Ionospheric Pierce Point (IPP) altitude of 350 km were obtained through the Ciraolo's calibration method (Ciraolo et al. 2007). For each GNSS station, at a specific time, a single vTEC value is obtained from the equivalent vTEC values calculated for each GPS satellite in view, whose number depends on the chosen minimum elevation angle. In this study, the cutoff elevation angle has been set to 20°.

vTEC time series have an original 30 s sampling; thus, they need to be uniformed to the *Nm*F2 15-min time sampling. This is why, vTEC values at minutes 0, 15, 30, and 45 of each hour were calculated following the Pignalberi et al. (2019) method. Specifically, windows centered at minutes 0, 15, 30, and 45 of each hour were applied to the 30 s vTEC time series, and only vTEC values falling in the window are used to calculate the weighted average vTEC value for that specific time. The Gaussian weight W_i here applied is defined as:

$$W_i = \exp\left[-\frac{(t_i - t_0)^2}{2\sigma^2}\right], \tag{1}$$

where $t_0 \in (0, 15, 30, 45)$ is the time of the center of the window, t_i is the time of each point falling in the window, and σ is a parameter acting as the variance in the Gaussian distribution; in our case, $\sigma = 150$ s (i.e., two and a half minutes). Once each vTEC value has been multiplied by the appropriate weight, the weighted mean $\overline{\text{vTEC}}$ is calculated and assigned to the center of the window according to the following relationship:

$$\overline{\text{vTEC}} = \frac{\sum_{i=1}^{N} \text{vTEC}_i \cdot W_i}{\sum_{i=1}^{N} W_i}, \tag{2}$$

where N is the number of values falling inside the window. Then, vTEC time series used in this study are 15-min weighted mean vTEC values.

2.2 Slab thickness calculation and binning

τ time series (expressed in meters) were calculated, for each station of Table 1, as the ratio between vTEC (expressed in el/m^2 and calculated as described in Sect. 2.1) and *Nm*F2 (expressed in el/m^3):

$$\tau = \frac{\text{vTEC}}{NmF2}, \tag{3}$$

at a 15 min time sampling, when both values were available. Since we are interested in describing the main climatological features of τ, only magnetically quiet conditions have been studied. To this task, several magnetic indices were investigated with different thresholds. After a preliminary study aiming at selecting the most suitable indices and thresholds, in order to get a balance between reliability and percentage of rejected data, the magnetic indices *Sym-H* and *AE* were selected. *Sym-H* (http://isgi.unistra.fr/Documents/References/Iyemori_et_al_2010.pdf) index gives information about magnetic disturbances observed on the ground at low and midlatitudes caused by the ring current, the partial ring current and by magnetopause and magnetotail currents during magnetic storms. Differently, *AE* index (Rostoker 1972) represents the total intensity of the auroral electrojets and gives information about the disturbance observed at high latitudes due to geomagnetic substorms. Such high-latitude disturbances can influence the midlatitude ionospheric composition (Prölss 1995). Then, *Sym-H* and *AE* indices complement each other. Magnetic activity indices, at 1-min interval, were downloaded from OMNIWeb Data Explorer website (https://spdf.gsfc.nasa.gov/pub/data/omni/high_res_omni/).

τ values used in this study are those calculated at the time t_0 for which is -25 nT $\leq$ *Sym-H* ≤ 5 nT and *AE* ≤ 300 nT (Kauristie et al. 2017). Time lags of one hour $[t_0 - 1\text{ h}, t_0]$ and two hours $[t_0 - 2\text{ h}, t_0]$, between magnetic data and τ time series, were also investigated for the above thresholds, but no significant differences have been found. Then, the magnetic filtering was applied according to the time of τ. As reported in Table 3, about 34% of the original τ dataset was discarded after applying the magnetic filtering.

The solar activity dependence has been studied by binning τ time series for three solar activity ranges (3 bins) based on the F10.7$_{81}$, i.e., the 81-day running mean of the F10.7 solar index. F10.7 daily data were downloaded at the NASA's OMNIWeb Data Explorer website (https://omniweb.gsfc.nasa.gov/form/dx1.html). F10.7 is the solar radio flux at 10.7 cm wavelength (2800 MHz) (Tapping 2013) and represents one of the most used solar activity proxy for ionospheric modeling. In particular, its 81-day running mean has been used in order to smooth its short-time variability we are not interested in for this climatological study. The solar activity binning is as follows:

- Low solar activity: F10.7$_{81}$ < 80 s.f.u. (solar flux unit, 1 s.f.u. = 10^{-22} Wm^{-2} Hz^{-1});
- Medium solar activity: 80 s.f.u. $\leq$ F10.7$_{81}$ < 120 s.f.u.;
- High solar activity: F10.7$_{81}$ $\geq$ 120 s.f.u.

Figure 1 depicts the F10.7$_{81}$ time series from 1965 to 2019, where the years (1997–2019) interested by our analysis are highlighted in light blue. Table 3 shows the percentage of data

Table 3 For each considered station, the percentage of the dataset rejected after applying the magnetic filtering to select quiet periods is reported

Station	Years dataset	Rejected data due to magnetic filtering [%]	Low solar activity [%]	Medium solar activity [%]	High solar activity [%]
Chilton	1997–2019	34.31	32.02	32.44	35.54
Roquetes	1997–2019	34.31	32.02	32.44	35.54
Wallops Island	1999–2019	34.06	32.30	31.06	36.64

The last three columns show the percentage of data (those remaining after applying the magnetic filtering) falling in each solar activity bin

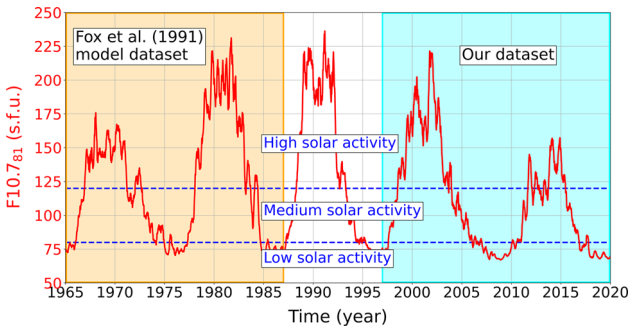

Fig. 1 F10.7$_{81}$ time series from 1965 to 2019. Years covered by our dataset (1997–2019) are highlighted in light blue, those covered by the Fox et al. (1991) dataset (1965–1986) in light orange. Blue horizontal dashed lines represent the chosen thresholds to perform a solar activity binning of the dataset

falling in each of the three solar activity bins (after applying the magnetic filtering), for each considered station. The chosen F10.7$_{81}$ thresholds allow for a quite uniform distribution of data in each of the three bins.

The seasonal dependence of τ is studied by binning data for each month of the year (12 bins), while the diurnal dependence is studied by binning data in bins fifteen-minute wide (96 bins), in local time (LT). So the total number of bins is 3(solar activity bins) $\times$ 12(months bins) $\times$ 96(diurnal bins) = 3456.

For each bin, several statistical quantities were calculated:

- Median, i.e., the 50th percentile;
- First quartile, i.e., the 25th percentile;
- Third quartile, i.e., the 75th percentile;
- Lower whisker, i.e., the 5th percentile;
- Upper whisker, i.e., the 95th percentile.

The median is considered the most appropriate statistical quantity when dealing with climatological studies being less affected by the tails of the distribution (outliers). The dispersion of data is estimated through the inter-quartile range (IQR), defined as the difference between the third and first quartile.

2.3 The Fox et al. (1991) equivalent slab thickness model for midlatitudes

Fox et al. (1991) developed a model describing the τ climatological behavior for midlatitudes. A detailed description of the model is given by Fox and Mendillo (1989), along with the Fortran77 code and needed coefficients for its implementation. For the purposes of this study, the Fortran77 code shared by Fox and Mendillo (1989) model has been translated in Python language.

The Fox et al. (1991) model is based on hourly *Nm*F2 ionosonde values recorded at Wallops Island (see Table 1) and vTEC data measured at Hamilton (Massachusetts, USA, 42.4° N, 70.5° W), from 1965 to 1986 (see Fig. 1 for the corresponding solar activity). vTEC data were obtained by observing the Faraday rotation of signals from the geosynchronous (GEO) satellites ATS-3 and ATS-5, at the IPP located at 420 km height (Fox et al. 1991).

As already mentioned in the introduction, Faraday rotation measurements can give the vTEC only up to 2000 km of altitude. Differently, vTEC values used in our analysis, being based on GNSS dual-frequency data, are instead representative of the ionosphere-plasmasphere system until about 20,000 km of altitude. In addition, vTEC obtained from GEO satellites are also affected by a local time smoothing effect, which might have significant effects around sunrise, due to the fact that, in general, the ray from the ground station to the satellite is not meridional but cuts through longitudes (Leitinger et al. 2004). These are all considerations that need to be taken into account in the following.

The Fox et al. (1991) model, through a weighted Fourier analysis, describes the climatological behavior of τ for different local times, months, and Sun Spot Number (SSN) values. Figure 2 shows some outputs of the model for different SSN values (from 0 to 250, with a step of 50), binned as a function of local time (hourly values) and month of the year. The model well describes the main climatological features of τ at midlatitudes. In particular, maximum τ values are found during daytime in summer, while smaller values can be observed in non-summer months, particularly during low solar activity, mostly during daytime than during nighttime. In winter, a post-sunset peak is observed, which delays its appearance

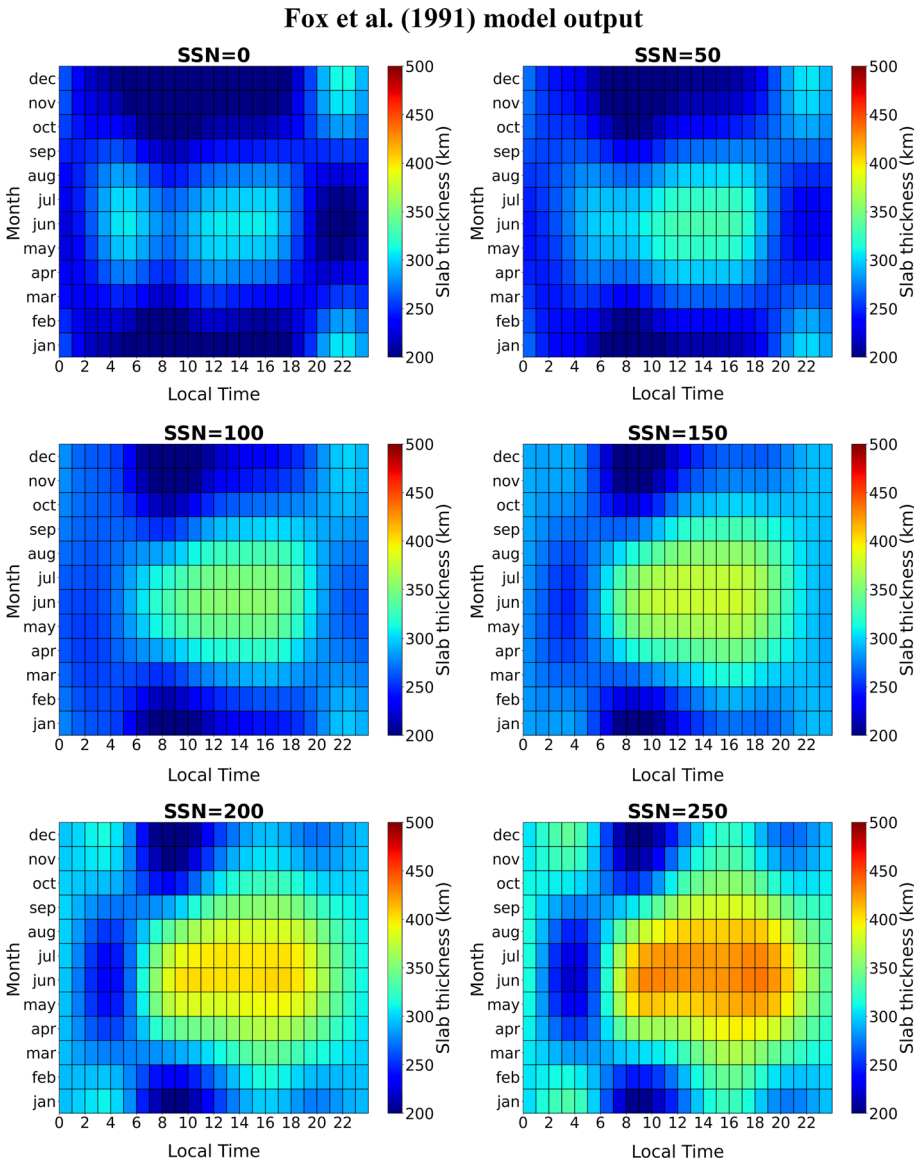

Fig. 2 Grids of τ values modeled by the Fox et al. (1991) model as a function of local time (x-axis), month of the year (y-axis), for different solar activity levels (SSN from 0 to 250, with a step of 50)

as the solar activity increases. Finally, an increase in τ with solar activity for all seasons at noontime is also evident.

It is worth highlighting that since the Fox et al. (1991) model was implemented, the SSN calculation method has changed. In particular, from the 1 June, 2015, a new version of SSN, replacing the oldest, has been released (Clette et al. 2015; Clette and Lefèvre 2016; Cliver 2016). This means that we could not use the new SSN (SSN_{new}) as input for the Fox et al. (1991) model, because such model requires the old SSN (SSN_{old}).

To properly compare modeled with measured τ values, at first, it is necessary to find a relation between $F10.7_{81}$ and SSN_{new}. SSN_{new} values were downloaded from the Sunspot Index and Long-term Solar Observations (SILSO) website (http://www.sidc.be/silso/home). To this regard, corresponding data from 1964 to 2019 were binned and a quadratic fit was performed (panel (c) of Fig. 3). The following relation is then assumed between $F10.7_{81}$ and SSN_{new}:

$$F10.7_{81} = a \cdot SSN_{new}^2 + b \cdot SSN_{new} + c, \tag{4}$$

where $a = -0.001$, $b = 0.729$, and $c = 68.094$. Through (4), it is possible to find the SSN_{new} value corresponding to $F10.7_{81}$.

Panel (a) of Fig. 3 shows the time series of SSN_{old} (also SSN_{old} values were downloaded from the SILSO website) and SSN_{new}, from the 1 January, 1964 to the 31 May, 2015, with the corresponding yearly running means, while panel (b) of Fig. 3 shows the corresponding ratio, which is evident not to be a simple constant. Panel (d) of Fig. 3 displays the density plot between SSN_{new} and SSN_{old}, which points out that a simple linear relation is sufficient to relate SSN_{new}

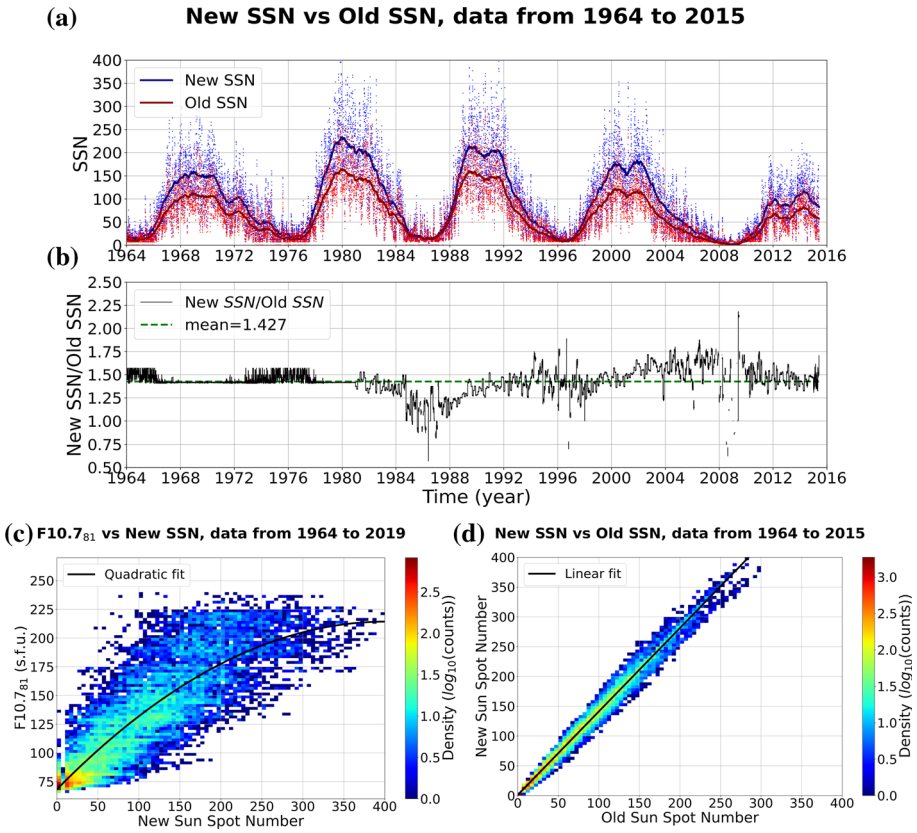

Fig. 3 **a** The SSN_{new} time series as blue dots, and the SSN_{old} time series as red dots, where blue and red solid curves represent corresponding yearly running mean. **b** Time series of the ratio between SSN_{new} and SSN_{old}, where the horizontal green dashed line represents the mean of the ratio along the entire time series. **c** Density plot between $F10.7_{81}$ and SSN_{new} time series (from 1964 to 2019). Black solid line represents the best quadratic fit. **d** Density plot between SSN_{new} and SSN_{old} (from 1964 to 2015), where the black solid line represents the best linear fit

to SSN_{old} in a satisfactory way; then, a linear fit has been performed:

$$SSN_{new} = a \cdot SSN_{old} + b, \tag{5}$$

where $a = 1.401$, and $b = 1.030$. Equation (5) allows switching from SSN_{new} to SSN_{old}.

Equations (4) and (5) allow to pass from the $F10.7_{81}$ value to the SSN_{old} value needed as input to the Fox et al. (1991) model to properly compare modeled and measured τ values corresponding to the three solar activity ranges defined in Sect. 2.2. Specifically, the SSN_{old} values are obtained as follows:

- Low solar activity $\rightarrow \overline{F10.7_{81}} = 72.26$ s.f.u. $\rightarrow SSN_{new} = 5.76 \rightarrow SSN_{old} = 3.38$;
- Medium solar activity $\rightarrow \overline{F10.7_{81}} = 98.17$ s.f.u. $\rightarrow SSN_{new} = 43.90 \rightarrow SSN_{old} = 30.60$;
- High solar activity $\rightarrow \overline{F10.7_{81}} = 153.38$ s.f.u. $\rightarrow SSN_{new} = 146.38 \rightarrow SSN_{old} = 103.75$;

where the mean values $\overline{F10.7_{81}}$ have been calculated by using $F10.7_{81}$ measurements from 1997 to 2019 falling in each of the three selected solar activity ranges (see Fig. 1). This means that our τ dataset can be compared with that modeled by Fox et al. (1991) by selecting $SSN_{old} = (3, 31, 104)$, respectively, for low, medium, and high solar activity. This will be the subject of Sect. 3.1.

3 Climatology of the equivalent slab thickness for midlatitude stations

3.1 Results for Wallops Island and comparison with the Fox et al. (1991) model

Since the Fox et al. (1991) model was developed by using a dataset of ionosonde measurements recorded at Wallops Island, a direct comparison with τ values measured at Wallops Island is fair. Nevertheless, the following not negligible differences have to be considered: vTEC values were obtained with different methodologies; the two datasets refer to different solar cycles; modeled τ values are a smoothed representation of the original dataset; the two datasets have a different time sampling.

Binned measured median τ values obtained for Wallops Island are compared with those modeled by Fox et al. (1991) according to the binning procedure described in Sect. 2.2. According to the different τ time series sampling, modeled Fox et al. (1991) values are binned hourly (in local time), while measured values are binned in 15-min wide bins.

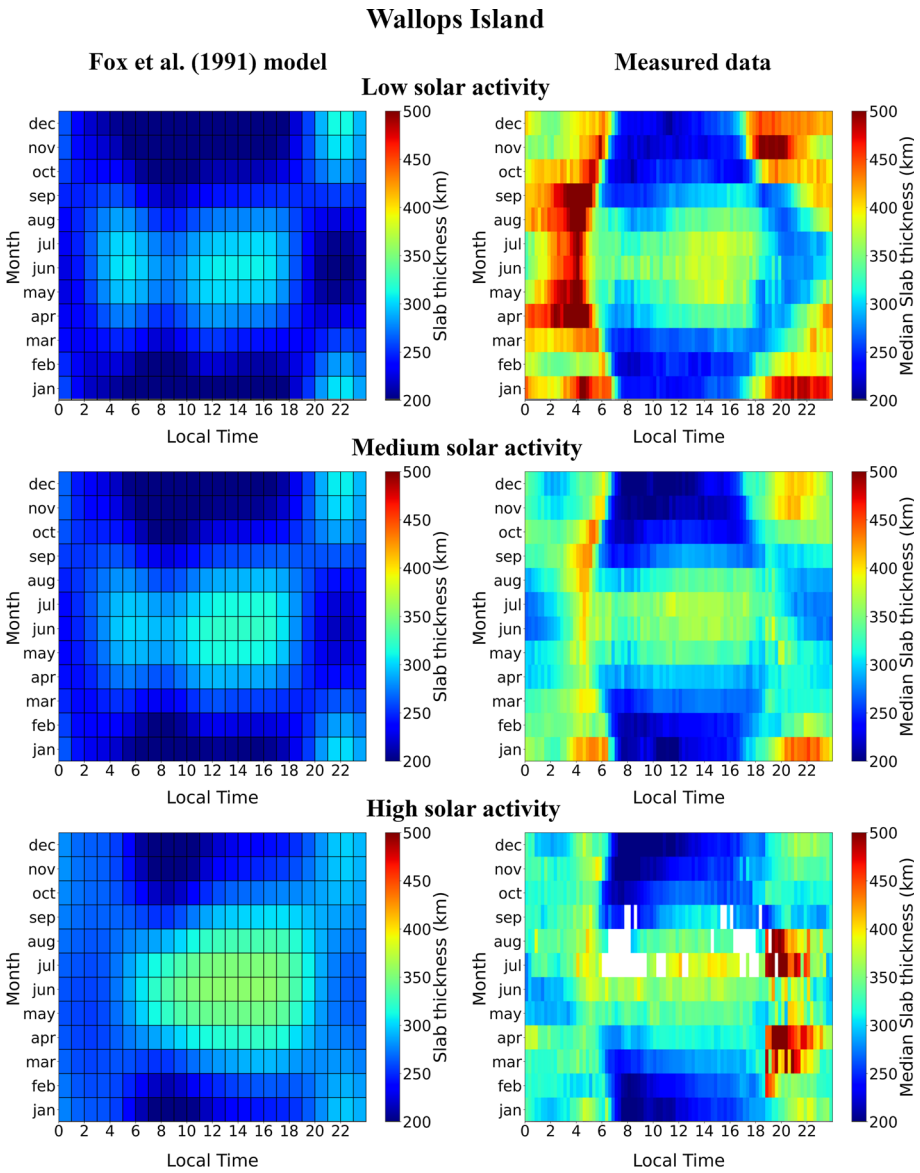

Fig. 4 (Left panels) Grids of 1 h binned equivalent slab thickness values modeled by Fox et al. (1991) at Wallops Island station, for low (first row), medium (second row), and high (third row) solar activity, as a function of local time (x-axis) and month of the year (y-axis). (Right panels) Corresponding grids of 15-min binned medians of equivalent slab thickness measurements. Empty bins are white colored

In Fig. 4, median τ values modeled by Fox et al. (1991) and corresponding measured median values are represented for Wallops Island for low, medium, and high solar activity. Measured median τ values are calculated when at least 10 values are present in the bin; this means that white bins visible for high solar activity are poorly populated and considered not statistically significant. In the Supporting Information material, in order to characterize the dispersion of τ around its median, we also provide the grids of IQR τ values (in the same layout of the right panels of Fig. 4); moreover, the grids of median *fo*F2 (from which *Nm*F2 values were obtained) and vTEC values, on which τ calculation is based, are provided to show their climatological trends.

The comparison between modeled and measured median τ values highlights several important differences:

(a) The most evident feature is the difference in terms of absolute value. Values modeled by Fox et al. (1991) are by far smaller than those measured, for both daytime and nighttime, and for different months. The most probable explanation is related to the different methodologies applied for calculating the vTEC. vTEC values obtained through Faraday rotation are inherently lower than those obtained by dual-frequency GNSS receivers, because of the smaller contribution given by the plasmasphere;

(b) Measured values are characterized by distinct maxima at solar terminator hours that are well highlighted, thanks to the 15-min time sampling of the measured data. Specifically, a dawn peak, particularly evident during low solar activity, for equinoctial and summer months, is observed. Such peak is a feature already found in

the past by several authors (Evans 1968; Titheridge 1973; Prasad et al. 1987). Concerning the modeled values, as described in Fox and Mendillo (1989), a weight inversely proportional to the quartile range of the individual hourly values was assigned to each bin of the model, and specifically, a lower weight was assigned to noisy bins, like those at dawn and dusk. This data treatment provided a smooth daily description of values that is likely at the base of the dawn peak removal. Nevertheless, this is not sufficient to justify the differences between modeled and measured values at these hours. In the literature, different explanations were given for this dawn peak (Bhonsle et al. 1965; Titheridge 1973; Jayachandra et al. 2004). A possible explanation has to be ascribed to the plasmaspheric contribution to vTEC values from GNSS. In fact, it is well known that remarkable differences arise between *Nm*F2 and vTEC (from GNSS) at night due to the plasma exchange between the ionosphere and the plasmasphere along the magnetic field lines (Klimenko et al. 2015). In addition, at solar terminator hours, the ionosphere is sunlit differently at different altitudes; then, *Nm*F2 and vTEC manifest a time lag which is well reflected in τ. For example, at dawn, higher values of τ mean that *Nm*F2 is low when vTEC is increasing due to the solar radiation impinging from above. The reverse is usually observed at dusk hours. This is particularly evident during equinoctial and summer months at low solar activity when *Nm*F2 at midlatitudes exhibits a characteristic maximum during evening hours (Zolesi and Cander 2014). Another explanation for the dawn peak relies on the observed morning increase (overshoot) of the electron temperature (Oyama et al. 1996, 1997) (usually called pre-sunrise peak) which, being by definition related to the plasma scale height, causes a corresponding increase in this (Stankov and Warnant 2009), and in the movement of the F2 layer due to either neutral winds (Titheridge 1973) or electrodynamics (Rastogi 1988). It is in fact observed that during early morning, the F2-layer peak height (*hm*F2) lowers by reaching a region characterized by higher recombination rates, then reducing *Nm*F2, and increasing τ;

(c) Modeled values exhibit a solar activity dependence, increasing as the solar activity increases (Fig. 2 and left panels of Fig. 4). It is not the same for measured values (right panels of Fig. 4). Since both *Nm*F2 and vTEC manifest a clear and similar solar activity dependence, one would expect that their ratio is unaffected from solar activity, and this is well confirmed during daytime hours. Instead, as the solar activity increases, a decreasing trend seems to characterize nighttime hours. Therefore, during nighttime, some further phenomena have to be considered to account for the exhibited behavior. An additional interesting feature that can be noted is the high values of τ observed for high solar activity, for some equinoctial and summer months, in the time interval 19–22 LT.

To further highlight the diurnal, seasonal, and solar activity variability of measured τ values at Wallops Island and also to show their dispersion around median values, corresponding boxplots are reported in Figs. 5a–c. For each of the three solar activity levels, we selected the months of March, June, September, and December as representative of the vernal equinox, summer solstice, autumn equinox, and winter solstice, respectively, and showed the corresponding diurnal trend.

Besides highlighting features already seen through Fig. 4, the boxplots give an immediate idea of the dispersion associated with median values. The main outcomes emerging from Figs. 5a–c are as follows:

(a) Nighttime and solar terminator hours are characterized by the highest dispersion, confirming the fact that at these hours, the role played by the plasmasphere is not negligible (Klimenko et al. 2015). During daytime, the F2 region gives the largest contribution to vTEC, and consequently *Nm*F2 and vTEC manifest very similar trends. The dispersion highlighted by IQR and whiskers well reflect all of these circumstances. It is worth highlighting that the analysis is based only on magnetically quiet periods, hence most of the dispersion arises from the peculiar day-to-day variability, which can be considered a second-order effect. When dealing with climatological analyses, only the diurnal, seasonal, and solar activity variability, that can be considered first-order effects, are highlighted;

(b) It is particularly evident that winter values are higher during nighttime than during daytime, probably due to the plasmaspheric plasma transport from the conjugate point in the summer hemisphere (Evans and Holt 1978);

(c) A dawn peak is a common feature shared by all seasons, particularly for low and medium solar activity;

(d) Comparing bins for the same hour and season, but for different solar activity, no clear solar activity dependence emerges;

(e) For March and September (equinoxes), τ presents a very similar behavior, especially for low and medium solar activity, as expected because both *Nm*F2 and vTEC exhibit the semi-annual anomaly (e.g., Rishbeth et al. 2000). Remarkable differences are instead observed between daytime values for summer and winter months, with higher values in summer.

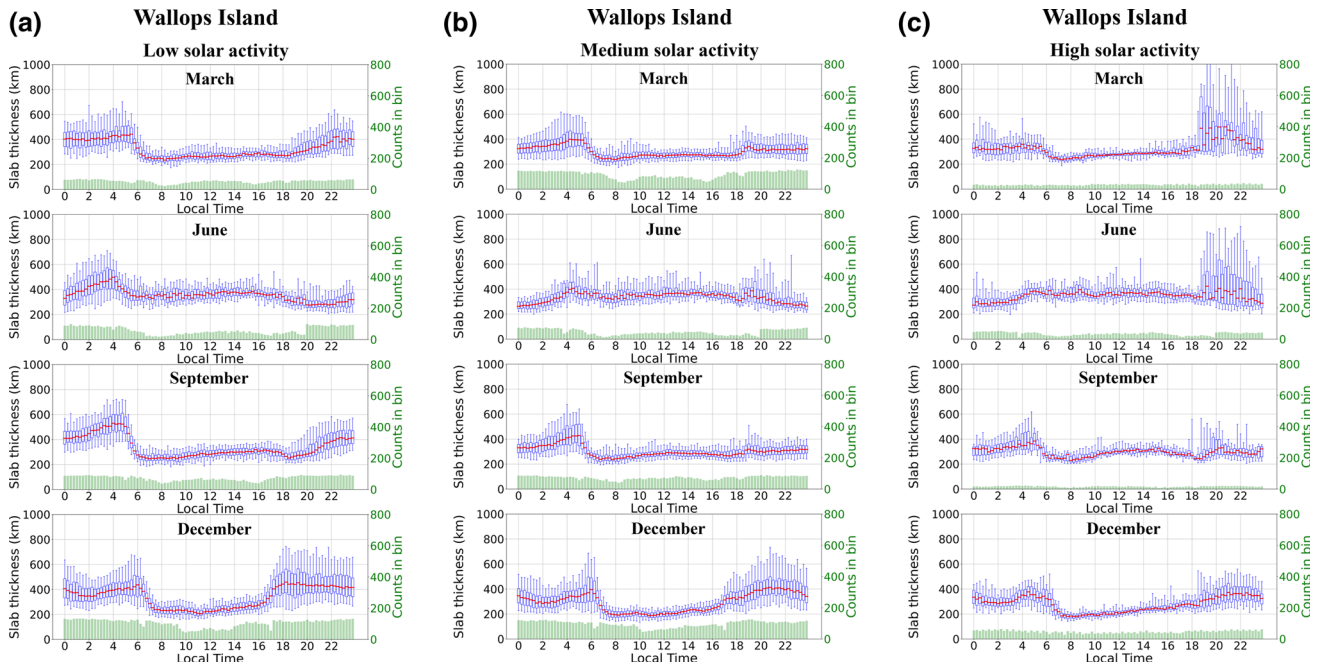

Fig. 5 **a** Measured equivalent slab thickness boxplots for Wallops Island. In each plot, data are binned as a function of the local time (15 min-wide bins), for March (vernal equinox), June (summer solstice), September (autumn equinox), and December (winter solstice), for low solar activity. For each bin, the red horizontal line represents the median of τ in that bin; the blue box represents the IQR, while the blue lines extending above and below the box are the whiskers. Green shaded bars at the bottom of each panel represent the number of values falling in that bin. **b** Same as **a** but for medium solar activity. **c** Same as **a** but for high solar activity

3.2 Results for the European sector: Chilton and Roquetes

The analysis performed for Wallops Island in the previous section is here extended to two European midlatitude stations: Chilton and Roquetes. These two stations are in the same longitudinal sector, so they give also the opportunity to study possible similarities and differences merely due to the latitude. Corresponding binned measured median τ values are shown in Fig. 6, for low, medium, and high solar activity. In the Supporting Information material, we provide also the grids of IQR τ values, and the grids of median *fo*F2 and vTEC values, for both Chilton and Roquetes.

From Fig. 6, some features emerge:

(a) Both at daytime in equinoctial (specifically, March and October) and winter months, and at nighttime (specifically, post-sunset hours) in the summer months, similar patterns characterized by very small values are observed independently of solar activity;
(b) Main differences are in the nighttime absolute values. Comparably higher values are observed at Roquetes (then at lower latitude) during the nighttime, above all for low solar activity and, except for summer months, also for medium solar activity. On the contrary, higher values during daytime characterize Chilton for the summer and equinoctial months independently of solar activity.

Figures 7a–c and 8a–c show the corresponding boxplots.

In order to provide an overall picture summarizing the τ behavior during daytime and nighttime, as well as around dawn and dusk hours, average values of medians represented in boxplots of Fig. 5a–c (Wallops Island), Fig. 7a–c (Chilton), and Fig. 8a–c (Roquetes), have been calculated for different LT sectors. Specifically, four different LT sectors have been considered:

- Dawn: [4:45,7:45] LT;
- Daytime: [8:00,16:30] LT;
- Dusk: [16:45,19:45] LT;
- Nighttime: [20:00,4:30] LT,

for low, medium, and high solar activity, and for the months of March, June, September, and December, representative of different seasons. Table 4 shows the corresponding results.

Figures 7a–c, 8a–c, and Table 4 show that:

(a) *Dawn hours* The largest differences for different solar activity levels observed for Chilton are 7, 6, 27, and 46 km in March, September, June and December, respectively; the corresponding values for Roquetes are

Table 4 Mean of the median values represented in boxplots of Fig. 5a–c (Wallops Island), Fig. 7a–c (Chilton), and Fig. 8a–c (Roquetes), for dawn, daytime, dusk, and nighttime, for the four months (March, June, September, December) representative of different seasons, and for the solar activity levels defined in Sect. 2.2

Solar activity level	Month	Diurnal sector	Wallops Island mean τ (km)	Chilton mean τ (km)	Roquetes mean τ (km)
Low solar activity	March	Dawn	291	315	297
		Daytime	246	251	238
		Dusk	261	250	223
		Nighttime	336	327	398
	June	Dawn	322	366	305
		Daytime	332	330	299
		Dusk	297	333	277
		Nighttime	315	271	264
	September	Dawn	293	304	272
		Daytime	261	266	251
		Dusk	256	255	225
		Nighttime	371	324	375
	December	Dawn	310	398	411
		Daytime	218	210	208
		Dusk	346	346	441
		Nighttime	343	308	436
Medium solar activity	March	Dawn	270	312	262
		Daytime	248	251	231
		Dusk	271	245	221
		Nighttime	296	304	323
	June	Dawn	315	355	308
		Daytime	329	336	312
		Dusk	306	322	272
		Nighttime	272	263	252
	September	Dawn	263	308	264
		Daytime	256	268	247
		Dusk	261	254	229
		Nighttime	299	283	305
	December	Dawn	258	385	341
		Daytime	193	196	190
		Dusk	289	355	376
		Nighttime	301	337	404
High solar activity	March	Dawn	260	308	267
		Daytime	264	257	252
		Dusk	291	257	255
		Nighttime	310	285	298
	June	Dawn	340	339	294
		Daytime	336	345	320
		Dusk	316	327	279
		Nighttime	278	275	253
	September	Dawn	265	302	257
		Daytime	272	279	250
		Dusk	253	255	232
		Nighttime	282	281	290
	December	Dawn	240	352	334
		Daytime	203	202	197
		Dusk	256	316	311
		Nighttime	290	364	423

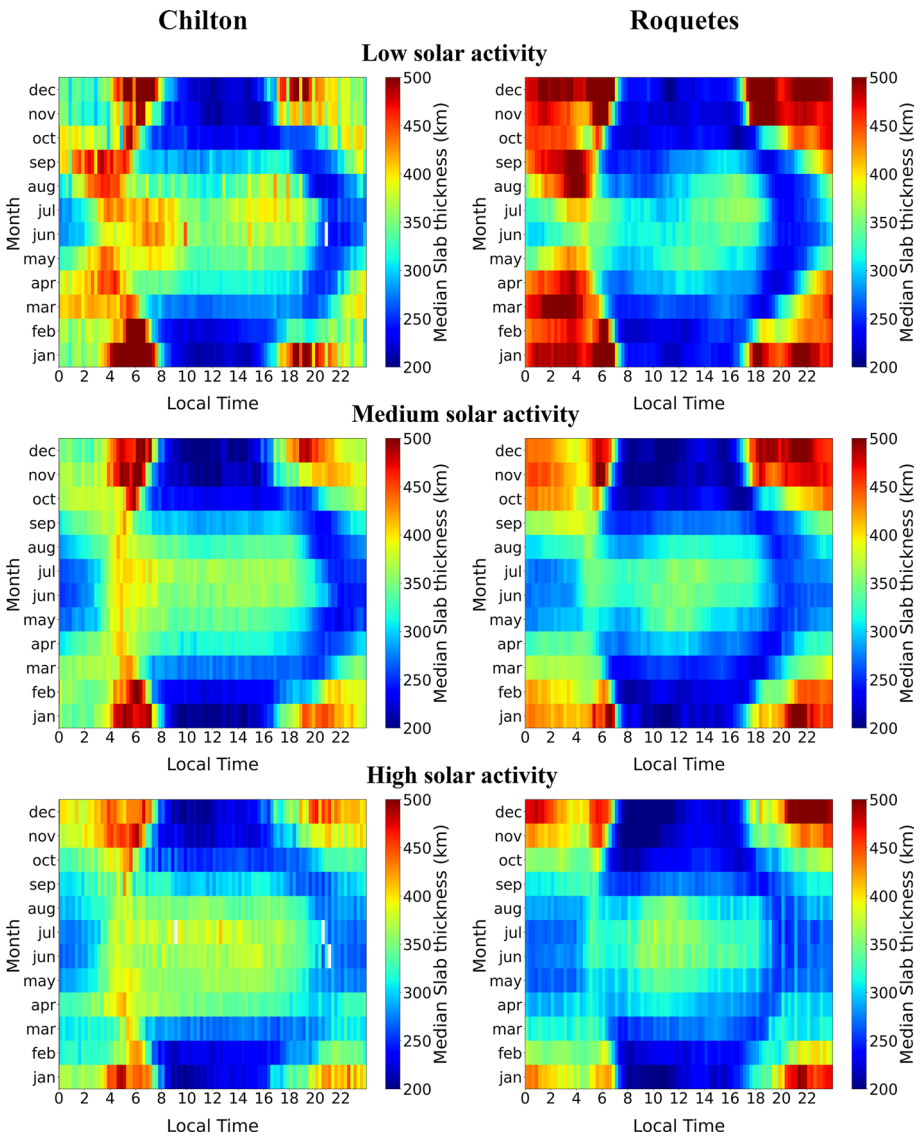

Fig. 6 Grids of 15 min-binned medians of equivalent slab thickness values measured at Chilton (left panels) and Roquetes (right panels), for low (first row), medium (second row), and high (third row) solar activity, as a function of local time (x-axis) and month of the year (y-axis). Empty bins are white colored

35, 15, 14, and 77 km. This means that at Chilton, in March and September, and at Roquetes in September and June, quite similar values of τ are observed independently of solar activity. Values slightly decrease as the solar activity increases in June at Chilton and in September at Roquetes. Decreasing trends as the solar activity level increases are observed to a greater extent in both stations in December. The comparison among values observed at Chilton and Roquetes in March, September, June, and December highlights that overall Chilton shows values by far larger than those obtained at Roquetes;

(b) *Daytime hours* The largest differences for different solar activity levels observed for Chilton are 6, 13, 15, and 14 km in March, September, June and December, respectively; the corresponding values for Roquetes are 14, 5, 21, and 18 km. This means that quite similar values are observed in all seasons for both Chilton and Roquetes independently of solar activity. Values slightly increase as the solar activity increases for June at both stations. The comparison among values observed at Chilton and Roquetes in March, September, June, and December shows that values at Chilton are always larger than those observed at Roquetes. These results fully agree with those found by Mosert et al. (2013) who, analyzing measurements from Pruhonice (50.0° N, 15.0° E, hence a station located at a latitude similar to that of Chilton) and Roquetes, during daytime (but also during nighttime) obtained higher values of τ for the station at higher latitude in winter, equinox, and summer;

(c) *Dusk hours* The largest differences for different solar activity levels observed for Chilton are 12, 1, 11, and 39 km in March, September, June, and December,

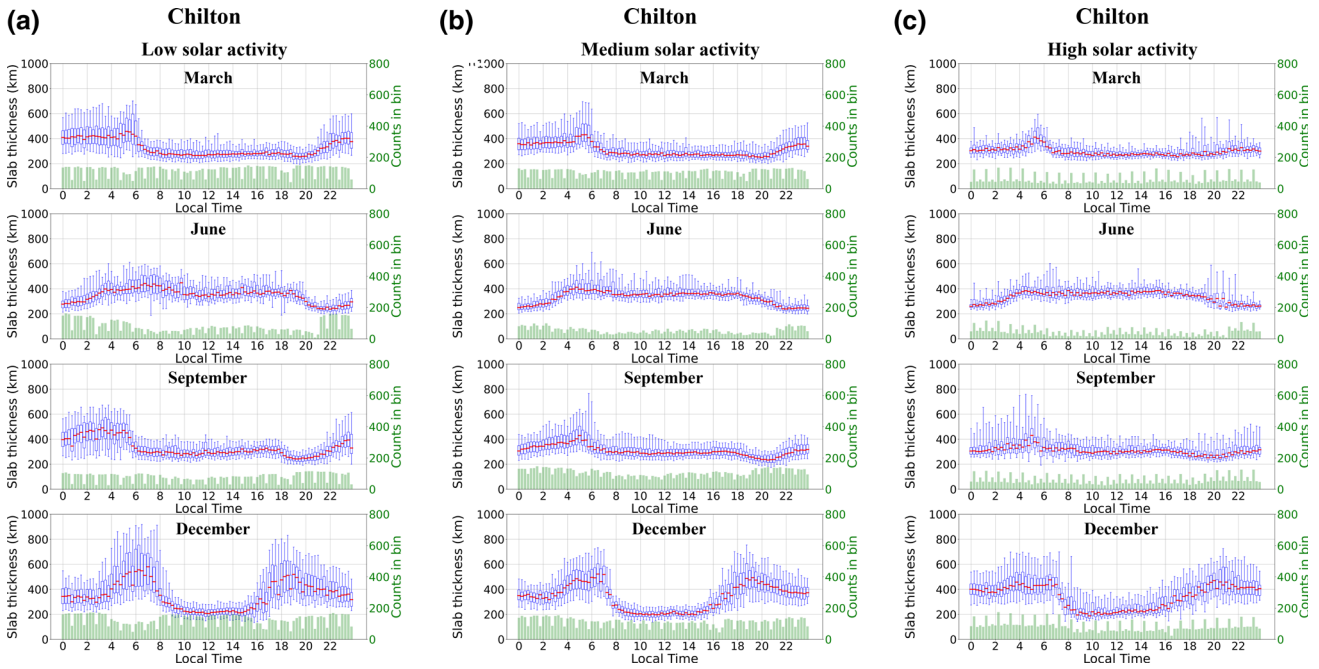

Fig. 7 **a** Same as Fig. 5a but for Chilton. **b** Same as Fig. 5b but for Chilton. **c** Same as Fig. 5c but for Chilton

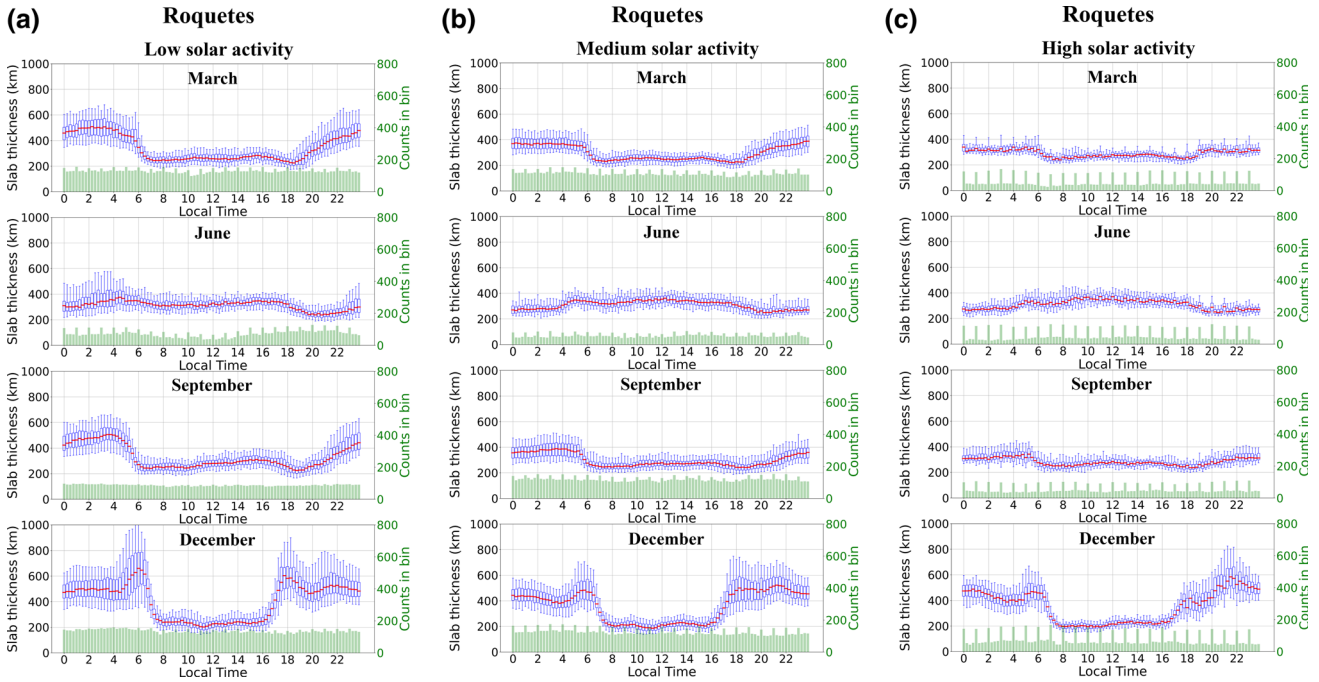

Fig. 8 **a** Same as Fig. 5a but for Roquetes. **b** Same as Fig. 5b but for Roquetes. **c** Same as Fig. 5c but for Roquetes

respectively; the corresponding values for Roquetes are 34, 6, 7, and 131 km. This means that at Chilton, in March, September, and June, and at Roquetes in September and June, quite similar values are observed independently of solar activity. Values clearly decrease as the solar activity increases in December at Roquetes. The comparison among values observed at Chilton and Roquetes highlights that overall Chilton shows values of τ by far larger than those observed at Roquetes;

(d) *Nighttime hours* The largest differences for different solar activity levels observed for Chilton are: 42, 43, 12, and 56 km in March, September, June, and December, respectively; the corresponding values for Roquetes are 100, 85, 12, and 32 km. Hence, differently from the day-

time hours, in March, September, and December, very different values depending on the solar activity level are observed for both stations. In particular, at Chilton, values clearly decrease as the solar activity increases in March and December, while at Roquetes values clearly decrease as the solar activity increases in March and September. It is noteworthy that the differences between values observed at Chilton and Roquetes highlight larger values for Roquetes, especially for low solar activity. Differently from the daytime hours, these results are opposite to those found by Mosert et al. (2013), which means that τ can behave in a multifaceted way with latitude;

(e) Both stations, except for June, during daytime hours, exhibit values remarkably smaller than those observed during nighttime hours, independently of the solar activity, especially for Roquetes. These results agree with those of Mosert et al. (2013) and Haralambous (2011) who analysing the τ behavior at the midlatitude stations of Roquetes and El Arenosillo (37.1° N, 6.7° W), for both solar minimum and maximum, and at the midlatitude station of Nicosia (35.0° N, 33.2° E) for low solar activity, respectively, found median τ daytime values smaller than nighttime ones during winter and equinoctial months. However, our results disagree with those of Jin et al. (2007) who, using the Korean GPS Network, found larger daytime values than nighttime ones during equinoxes. The physical mechanism that plays a crucial role in enhancing considerably the τ values during nighttime hours is mainly the field aligned plasma flow from the plasmasphere to the ionosphere (Minakoshi and Nishimuta 1994). Large downward fluxes of H^+ lower the upper transition height, that is the height where the percentage of O^+ is equal to the percentage of H^+, leading to an increase in the topside electron content during nighttime and then to an increase in τ, as observed by Evans and Holt (1978) in winter and in particular during post-midnight hours;

(f) Independently of solar activity, each station exhibits very similar trends in equinoctial months;

(g) Except in winter, during the early nighttime hours, for medium and high solar activity, Roquetes shows a constant trend, while an increasing trend is observed at Chilton;

(h) For both stations, the dispersion of values is by far larger during nighttime hours, with a tendency to be the largest at dawn and dusk;

(i) On the whole, both stations exhibit around dawn values larger than those observed around dusk, except for Roquetes in December, for both low and medium solar activity; in general, Chilton shows values much larger than those observed at Roquetes. The presence of a peak around dawn hours (also called pre-sunrise peak) is evident in the equinoctial months at Chilton, but not at Roquetes, and in particular in winter for both stations with the peak tending to be less pronounced as the solar activity increases; such feature agrees with the finding of Minakoshi and Nishimuta (1994) who detected a pre-sunrise peak for low solar activity, fading away as the solar activity increases and reappearing for high solar activity, particularly in winter. Actually, a τ peak around dawn hours is a feature that is observed rather frequently at midlatitude for low solar activity (Davies and Liu 1991; Jayachandran et al. 2004; Stankov and Warnant 2009; Haralambous 2011; Mosert et al. 2013), and also for high solar activity (Minakoshi and Nishimuta 1994; Stankov and Warnant 2009; Chuo et al. 2010), and this agrees with our results at Roquetes where the peak around dawn appears also for high solar activity. Moreover, the presence of a peak around dusk hours (also called post-sunset peak) observed especially in winter both at Chilton and Roquetes independently of solar activity is a phenomenon in agreement with the observations carried out by many authors (Jayachandran et al. 2004; Stankov and Warnant 2009; Chuo et al. 2010; Haralambous 2011; Mosert et al. 2013; Huang and Yuan 2015). From the physical point of view, the occurrence of both peaks is due to the electrodynamics of the F region; specifically, the combined effect of changes of meridional neutral winds direction (Titheridge 1973), most prominent in winter months (Krishna Murthy et al. 1990), and enhanced zonal electric fields cause the downward movement of the ionosphere leading to an increase in ion loss due to recombination. As a consequence, a decrease in *Nm*F2 much faster than that of the topside electron content occurs (Davies and Liu 1991). In addition, as previously said, a large field aligned plasma flow from the protonosphere can decrease the upper transition height especially in winter, thus increasing the topside content during nighttime; a phenomenon that Evans and Holt (1978) observed in particular in winter during the post-midnight hours. Thereby the simultaneous depletion of *Nm*F2 and enhancement of the topside content would explain both peaks observed in the winter season. In other terms, the presence of pre-sunrise and post-sunset peaks, as observed in winter at Chilton and Roquetes, reflects primarily the plasmaspheric variation (e.g., Belehaki et al. 2003) characterized by a double peak at dawn and at dusk caused by the lowering of the upper transition height, which in winter is most significant;

(j) For both stations, during daytime hours, values observed in winter are considerably smaller than those observed in summer, which means that the winter anomaly characterizing both *fo*F2 and vTEC is not reflected in τ.

3.3 Comparison between Chilton and Wallops Island

Although Chilton and Wallops Island stations are at a very different geographic latitude (51.5° N Chilton, 37.9° N Wallops Island), in Quasi-Dipole (QD) magnetic coordinates (Laundal and Richmond 2017), they are on the same parallel (47.8° N Chilton, 47.7° N Wallops Island), which stimulated us to make a comparison between the two. The comparison shows similar features both in terms of diurnal and seasonal behavior and absolute values, which was somewhat expected in virtue of the same geomagnetic latitude of the two stations. Nevertheless, from a careful inspection of the climatological results obtained for Wallops Island (Fig. 4, right panels) and Chilton (Fig. 6, left panels), some differences come out:

1. for low solar activity, the dawn peak is more pronounced at Wallops Island in equinoctial and summer months and at Chilton in winter months. For medium solar activity, the dawn peak is similar in summer, but it is more prominent at Chilton in winter. For high solar activity, the dawn peak tends to fade out at Wallops Island, while it is still observed at Chilton;
2. for high solar activity, very high values of τ are observed at Wallops Island in equinoctial and summer months in the time interval 19–22 LT. Such feature is not present at Chilton.

Figures 5a–c, 7a–c, and Table 4 show that:

(a) *Dawn hours* The largest differences for different solar activity levels observed for Wallops Island are 31, 30, 25, and 70 km in March, September, June, and December, respectively; the corresponding values for Chilton are 7, 6, 27, and 46 km. This means that at Wallops Island, τ is more sensitive to the solar activity than at Chilton. Like Chilton, also Wallops Island shows values decreasing as the solar activity increases in December. The difference between values indicates that at Chilton, τ is by far larger than at Wallops Island independently of solar activity and season;

(b) *Daytime hours* The largest differences for different solar activity levels observed for Wallops Island are 18, 16, 7, and 25 km in March, September, June, and December, respectively; the corresponding values for Chilton are 6, 13, 15, and 14 km. This means that quite similar values are observed independently of solar activity. No clear dependence on the solar activity is observed;

(c) *Dusk hours* The largest differences for different solar activity levels observed for Wallops Island are 30, 8, 19, and 90 km in March, September, June, and December, respectively; the corresponding values for Chilton are 12, 1, 11, and 39 km. This means that similarly to Chilton, in September and June, at Wallops Island, quite similar values are observed independently of solar activity. On the contrary, in December, at Wallops Island, values significantly decrease as the solar activity increases;

(d) *Nighttime hours* The largest differences for different solar activity levels observed for Wallops Island are 40, 89, 43, and 53 km in March, September, June and December, respectively; the corresponding values for Chilton are 42, 43, 12, and 56 km. Hence, unlike daytime, for all months, values show a dependence on the solar activity. In particular, at Wallops Island, values decrease as the solar activity increases in September and December. The differences between values observed at Chilton and Wallops Island highlight that at Wallops Island values are larger than those observed at Chilton for low solar activity; while in winter, for both medium and high solar activity, values are larger at Chilton;

(e) Wallops Island, during daytime, exhibits values remarkably smaller than those observed during nighttime, specifically for equinoctial months and in winter independently of solar activity; this feature is more evident at Wallops Island than at Chilton for equinoctial months and in winter for low solar activity, while in winter for both medium and high solar activity is the contrary. Similarly to Chilton, in June, at Wallops Island, daytime values are greater than nighttime ones.

4 Conclusive remarks

The main purpose of the present study was to investigate the climatological behavior of the equivalent slab thickness for midlatitudes, for quiet geomagnetic conditions. Empirical climatological models like the International Reference Ionosphere (IRI, Bilitza et al. 2017) and NeQuick (Nava et al. 2008) could take advantage from the use of the slab thickness parameter to better describe the shape of the vertical electron density profile of the ionosphere. For this task, the climatological results obtained in this paper might be of help.

Specifically, in this work, we analyzed the equivalent slab thickness climatological behavior as observed at three midlatitude stations located in the Northern hemisphere (North-American and European sectors). The main obtained results are as follows:

- Measured values are characterized by distinct maxima at solar terminator hours, a feature that is not highlighted by the Fox et al. (1991) model;
- Fox et al. (1991) modeled values exhibit a solar activity dependence, independently of the LT, increasing as the solar activity increases. Measured values instead show a different behavior depending on whether they are daytime or nighttime values; daytime values do not show any

dependence on solar activity, while a slight decreasing trend seems to characterize nighttime values as the solar activity increases;
- Another interesting feature, not highlighted by the Fox et al. (1991) model, is the presence of high values observed for high solar activity, for some equinoctial and summer months, in the LT sector 19–22;
- Except for June, daytime values are remarkably smaller than nighttime ones, independently of solar activity;
- Nighttime and solar terminator hours are characterized by the highest dispersion, confirming the fact that at these hours, the role played by the plasmasphere is not negligible;
- The analyses related to stations at the same geomagnetic latitude, but in different longitude sectors, show some difference, as well as those related to stations at different latitudes.

The methodology employed about data selection, filtering, and binning procedures is particularly suited for modeling purposes and constitutes a preliminary step for the implementation of local slab thickness climatological models. These models might be developed using the datasets here presented so as to provide for midlatitudes a faithful description of both the diurnal and seasonal variability of τ for different solar activity levels. It is intention of the authors to explore this possibility in the future. Moreover, since the comparison between stations located at the same geomagnetic latitude shows some difference, it is also intention of the authors to extend this analysis to different latitude sectors for both Northern and Southern hemispheres. Furthermore, as shown here and in the literature, τ exhibits a dependence on the magnetic latitude. The extension of this study to low and high latitudes is valuable to investigate the slab thickness climatological patterns also at these latitudes, with the aim to test the possibility of developing a global model.

Supplementary Information The online version contains supplementary material available at https://doi.org/10.1007/s00190-021-01577-7.

Acknowledgements This publication uses data from ionospheric observatories made available via the public access portal of the Digital Ionogram Database (http://ulcar.uml.edu/DIDBase/) of the Global Ionosphere Radio Observatory in Lowell, MA. The authors are indebted to the observatory directors and ionosonde operators for the significant investments of their time, effort, expertise, and funds needed to acquire and provide measurement data to academic research. Thanks to the International GNSS Service (IGS, http://www.igs.org/) team for providing and making freely available GNSS data, and for their huge efforts in setting, maintaining, and developing their GNSS stations network. RINEX files used in this study were downloaded from NASA's GNSS repository (https://cddis.nasa.gov/Data_and_Derived_Products/CDDIS_Archive_Access.html). The authors thank Dr. Luigi Ciraolo for providing us a tailored version of his vTEC calibration software. Magnetic activity indices used in this study were downloaded from NASA's Space Physics Data Facility of the Goddard Space Flight Center (https://spdf.gsfc.nasa.gov/pub/data/omni/high_res_omni/). The $F_{10.7}$ solar index was downloaded through OMNIWeb Data Explorer website (https://omniweb.gsfc.nasa.gov/form/dx1.html) maintained by the NASA. SSN_{new} and SSN_{old} solar indices were downloaded from Sunspot Index and Long-term Solar Observations (SILSO) website (http://www.sidc.be/silso/home).

Author contributions AP contributed to conceptualization, methodology, software, validation, formal analysis, investigation, and writing-original draft. BN contributed to conceptualization, writing-review and editing, investigation, and validation. MPi contributed to writing-original draft, investigation, and validation. CC contributed to writing-review and editing, investigation, and validation. MPe contributed to supervision, writing-review and editing, funding acquisition, investigation, and validation.

Funding This research is partially supported by the Italian MIUR-PRIN grant 2017APKP7T on Circumterrestrial Environment: Impact of Sun-Earth Interaction.

Data availability Ionosondes' data are available via the public access portal of the Digital Ionogram Database (http://ulcar.uml.edu/DIDBase/) of the Global Ionosphere Radio Observatory in Lowell. RINEX files are available from NASA's GNSS FTP repository (ftp://cddis.nasa.gov/). Magnetic activity indices are available from NASA's Space Physics Data Facility of the Goddard Space Flight Center (https://spdf.gsfc.nasa.gov/pub/data/omni/high_res_omni/). Solar activity indices are available from OMNIWeb Data Explorer website (https://omniweb.gsfc.nasa.gov/form/dx1.html) and from Sunspot Index and Long-term Solar Observations (SILSO) website (http://www.sidc.be/silso/home). Slab thickness datasets generated in this study are available from the corresponding author on reasonable request.

References

Belehaki A, Jakowski N, Reinisch BW (2003) Comparison of ionospheric ionization measurements over Athens using ground ionosonde and GPS-derived TEC values. Radio Sci 38(6):1–11. https://doi.org/10.1029/2003RS002868

Bhonsle R V, Da Rosa AV, Garriott OK (1965) Measurements of the total electron content and the equivalent stab thickness of the mid-latitude ionosphere. Radioscience Laboratory, Stanford University, Stanford, California, USA. https://ntrs.nasa.gov/archive/nasa/casi.ntrs.nasa.gov/19660006131.pdf

Bibl K, Reinisch BW (1978) The universal digital ionosonde. Radio Sci 13:519–530. https://doi.org/10.1029/RS013i003p00519

Bilitza D, Altadill D, Truhlik V, Shubin V, Galkin I, Reinisch BW, Huang X (2017) International reference ionosphere 2016: from ionospheric climate to real-time weather predictions. Space Weather 15:418–429. https://doi.org/10.1002/2016SW001593

Breed AM, Goodwin GL, Vandenberg AM, Essex EA, Lynn KJW, Silby JH (1997) Ionospheric total electron content and slab thickness determined in Australia. Radio Sci 32(4):1635–1643. https://doi.org/10.1029/97RS00454

Chuo YJ, Lee CC, Chen WS (2010) Comparison of ionospheric equivalent slab thickness with bottomside digisonde profile over Wuhan. J Atmos Solar Terr Phy 72:528–533. https://doi.org/10.1016/j.jastp.2010.02.003

Ciraolo L, Azpilicueta F, Brunini C, Meza A, Radicella SM (2007) Calibration errors on experimental slant total electron content (TEC) determined with GPS. J Geodesy 81(2):111–120. https://doi.org/10.1007/s00190-006-0093-1

Clette F, Svalgaard L, Vaquero JM, Cliver EW (2015) Revisiting the sunspot number. In: Balogh A, Hudson H, Petrovay K, von Steiger R (eds) The solar activity cycle. Space sciences series of ISSI, vol 53. Springer, New York

Clette F, Lefèvre L (2016) The new sunspot number: assembling all corrections. Sol Phys 291:2629–2651. https://doi.org/10.1007/s11207-016-1014-y

Cliver EW (2016) Comparison of new and old sunspot number time series. Sol Phys 291:2891–2916. https://doi.org/10.1007/s11207-016-0929-7

Dabas RS, Bhuyan PK, Tyagi TR, Bharadwaj PK, Lal JB (1984) Day-to-day changes in ionospheric electron content at low-latitudes. Radio Sci 19:749–756. https://doi.org/10.1029/RS019i003p00749

Davies K (1990) Ionospheric radio. Peter Peregrinus Ltd., London, United Kingdom

Davies K, Liu XM (1991) Ionospheric slab thickness in middle and low-latitudes. Radio Sci 26(4):997–1005. https://doi.org/10.1029/91RS00831

Evans JV (1968) Sunrise behavior of the F layer at mid-latitudes. J Geophys Res 73(11):3489–3504. https://doi.org/10.1029/JA073i011p03489

Evans JV, Holt JM (1978) Night time proton flux at Millstone Hill. Planet Space Sci 26(8):727–744. https://doi.org/10.1016/0032-0633(78)90004-1

Fox MW, Mendillo M, Klobuchar JA (1991) Ionospheric equivalent slab thickness and its modeling applications. Radio Sci 26(2):429–438. https://doi.org/10.1029/90RS02624

Fox MW, Mendillo M (1989) Ionospheric equivalent slab thickness and its modeling applications. Scientific report n.2, Boston University, Boston, Massachusetts. https://pdfs.semanticscholar.org/c628/f20aac55df83a9cd31f05e06cb9a0c412485.pdf

Froń A, Galkin I, Krankowski A, Bilitza D, Hernández-Pajares M, Reinisch B, Li Z, Kotulak K, Zakharenkova I, Cherniak I, Roma Dollase D, Wang N, Flisek P, García-Rigo A (2020) Towards cooperative global mapping of the ionosphere: fusion feasibility for IGS and IRI with global climate VTEC maps. Remote Sens 12(21):3531. https://doi.org/10.3390/rs12213531

Galkin IA, Reinisch BW (2008) The new ARTIST 5 for all digisondes. Ionosonde Network advisory group bulletin 69. http://www.ips.gov.au/IPSHosted/INAG/web-69/2008/artist5-inag.pdf

Gerzen T, Jakowski N, Wilken V, Hoque MM (2013) Reconstruction of F2 layer peak electron density based on operational vertical total electron content maps. Ann Geophys 31:1241–1249. https://doi.org/10.5194/angeo-31-1241-2013

Goodwin GL, Silby JH, Lynn KJW, Breed AM, Essex EA (1995) GPS satellite measurements: ionospheric slab thickness and total electron content. J Atmos Terr Phys 57:1723–1732. https://doi.org/10.1016/0021-9169(95)00093-H

Haralambous H (2011) Investigation of ionospheric slab thickness behavior over cyprus during minimum solar activity. In: PIERS proceedings, Marrakesh, Morocco, March 20–23, 2011

Huang Z, Yuan H (2015) Climatology of the ionospheric slab thickness along the longitude of 120° E in China and its adjacent region during the solar minimum years of 2007–2009. Ann Geophys 33:1311–1319. https://doi.org/10.5194/angeo-33-1311-2015

Jakowski N, Hoque MM (2021) Global equivalent slab thickness model of the earth's ionosphere. J Space Weather Space Clim 11:10. https://doi.org/10.1051/swsc/2020083

Jakowski N, Hoque MM, Mielich J, Hall C (2017) Equivalent slab thickness of the ionosphere over Europe as an indicator of long-term temperature changes in the thermosphere. J Atmos Sol Terr Phys 163:91–102. https://doi.org/10.1016/j.jastp.2017.04.008

Jayachandran B, Krishnankutty TN, Gulyaeva TL (2004) Climatology of ionospheric slab thickness. Ann Geophys 22:25–33. https://doi.org/10.5194/angeo-22-25-2004

Jin S, Cho JH, Park JU (2007) Ionospheric slab thickness and its seasonal variation observed by GPS. J Atmos Sol Terr Phys 69:1864–1870. https://doi.org/10.1016/j.jastp.2007.07.008

Kauristie K, Morschhauser A, Olsen N, Finlay CC, McPherron RL, Gjerloev JW, Opgenoorth HJ (2017) On the usage of geomagnetic indices for data selection in internal field modelling. Space Sci Rev 206:61–90. https://doi.org/10.1007/s11214-016-0301-0

Klimenko MV, Klimenko VV, Zakharenkova IE, Cherniak V (2015) The global morphology of the plasmaspheric electron content during northern winter 2009 based on GPS/COSMIC observation and GSM TIP model results. Adv Space Res 55(8):2077–2085. https://doi.org/10.1016/j.asr.2014.06.027

Krankowski A, Shagimuratov II, Baran LW (2007) Mapping of foF2 over Europe based on GPS-derived TEC data. Adv Space Res 39(5):651–660. https://doi.org/10.1016/j.asr.2006.09.034

Krishna Murthy BK, Hari SS, Somayajulu VV (1990) Nighttime equatorial thermospheric merdional winds from ionospheric h'F data. J Geophys Res 95:4307–4310. https://doi.org/10.1029/JA095iA04p04307

Laundal KM, Richmond AD (2017) Magnetic coordinate systems. Space Sci Rev 206:27. https://doi.org/10.1007/s11214-016-0275-y

Leitinger L, Ciraolo L, Kersley L, Kouris SS, Spalla P (2004) Relations between electron content and peak density-regular and extreme behavior. Ann Geophys 47(2/3):1093–1107. https://doi.org/10.4401/ag-3287

Minakoshi H, Nishimuta I (1994) Ionospheric electron content and equivalent slab thickness at lower mid latitudes in the Japanese zone. In: Proc. beacon satellite symposium (IBSS), 144, Wales, UK

Mosert M, Magdaleno S, Buresova D, Altadill D, Gende M, Gularte E, Scida L (2013) Behavior of the equivalent slab thickness over three European stations. Adv Space Res 51(4):677–682. https://doi.org/10.1016/j.asr.2012.06.002

Nava B, Coïsson P, Radicella SM (2008) A new version of the NeQuick ionosphere electron density model. J Atmos Sol Terr Phys 70:1856–1862. https://doi.org/10.1016/j.jastp.2008.01.015

Nava B, Radicella SM, Azpilicueta F (2011) Data ingestion into NeQuick 2. Radio Sci 46:RS0D17. https://doi.org/10.1029/2010RS004635

Oyama KI, Balan N, Watanabe S, Takahashi T, Isoda F, Bailey GJ, Oya H (1996) Morning overshoot of Te enhanced by downward plasma drift in the equatorial topside ionosphere. J Geomagn Geoelectr 48:959–966. https://doi.org/10.5636/jgg.48.959

Oyama KI, Abdu MA, Balan N, Bailey GJ, Watanabe S, Takahashi T, Paula ER, Batista IS, Isoda F, Oya H (1997) High electron temperature associated with the prereversal enhancement. J Geophys Res 102:417–424. https://doi.org/10.1029/96JA02705

Pezzopane M, Del Corpo A, Piersanti M, Cesaroni C, Pignalberi A, Di Matteo S, Spogli L, Vellante M, Heilig B (2019) On some features characterizing the plasmasphere–magnetosphere–ionosphere system during the geomagnetic storm of 27 May 2017. Earth Planets Space 71:77. https://doi.org/10.1186/s40623-019-1056-0

Pezzopane M, Scotto C (2005) The INGV software for the automatic scaling of foF2 and MUF(3000)F2 from ionograms: a performance comparison with ARTIST 4.01 from Rome data. J Atmos Sol-Terr Phys 67(12):1063–1073. https://doi.org/10.1016/j.jastp.2005.02.022

Pezzopane M, Scotto C (2007) Automatic scaling of critical frequency foF2 and MUF(3000)F2: a comparison between autoscala and ARTIST 4.5 on rome data. Radio Sci. 42:RS4003. https://doi.org/10.1029/2006RS003581

Pignalberi A, Pezzopane M, Rizzi R (2018) Modeling the lower part of the topside ionospheric vertical electron density profile over the European region by means of Swarm satellites data and IRI UP method. Space Weather. https://doi.org/10.1002/2017SW001790

Pignalberi A, Habarulema JB, Pezzopane M, Rizzi R (2019) On the development of a method for updating an empirical climatological ionospheric model by means of assimilated vTEC measurements from a GNSS receiver network. Space Weather 17:1131–1164. https://doi.org/10.1029/2019SW002185

Pignalberi A, Pezzopane M, Themens DR, Haralambous H, Nava B, Coïsson P (2020a) On the analytical description of the topside ionosphere by nequick: modeling the scale height through COSMIC/FORMOSAT-3 selected data. IEEE J Select Top Appl Earth Obs Remote Sens 13:1867–1878. https://doi.org/10.1109/JSTARS.2020.2986683

Pignalberi A, Pezzopane M, Nava B, Coïsson P (2020b) On the link between the topside ionospheric effective scale height and the plasma ambipolar diffusion, theory and preliminary results. Sci Rep 10(1):17541. https://doi.org/10.1038/s41598-020-73886-4

Pignalberi A, Pietrella M, Pezzopane M, Habarulema JB (2021) Investigating different vTEC calibration methods for data assimilation in ionospheric empirical models. Adv Space Res 68(5):2138–2151. https://doi.org/10.1016/j.asr.2020.10.040

Prasad DSVVD, Niranjan K, Rama Rao PVS (1987) TEC and equivalent slab thickness at low and mid-latitudes - a comparative study. Ind. J. Radio Space Phys. 16:295–299. http://nopr.niscair.res.in/bitstream/123456789/36503/1/IJRSP%2016%284%29%20295-299.pdf

Prölss GW (1995) Ionospheric F-region storms. In: Volland H (ed) Handbook of atmospheric electrodynamics, vol 2. CRC Press, Boca Raton, pp 195–248

Rastogi RG (1988) Collapse of the equatorial ionosphere during the sunrise period. Ann. Geophys. 6:205. https://www.prl.res.in/~library/rg_rastogi_6_2_205_1988.pdf

Reinisch BW, Galkin I (2011) Global Ionospheric Radio observatory (GIRO). Earth Planets Space 63(4):377–381. https://doi.org/10.5047/eps.2011.03.001

Rishbeth H, Müller-Wodarg ICF, Zou L, Fuller-Rowell TJ, Millward GH, Moffett RJ, Idenden DW, Aylward AD (2000) Annual and semiannual variations in the ionospheric F2-layer: II. Phys Discuss Ann Geophys 18(8):945–956. https://doi.org/10.1007/s00585-000-0945-6

Rostoker G (1972) Geomagnetic Indices. Rev Geophys Space Phys 10:157. https://doi.org/10.1029/RG010i004p00935

Stankov SM, Jakowski N (2006) Topside ionospheric scale height analysis and modelling based on radio occultation measurements. J Atmos Sol-Terr Phys 68(2):134–162. https://doi.org/10.1016/j.jastp.2005.10.003

Stankov SM, Warnant R (2009) Ionospheric slab thickness - analysis, modelling and monitoring. Adv Space Res 44:1295–1303. https://doi.org/10.1016/j.asr.2009.07.010

Tapping KF (2013) The 10.7 cm solar radio flux ($F_{10.7}$). Space Weather 11:394–406. https://doi.org/10.1002/swe.20064

Titheridge JE (1972) Determination of ionospheric electron content from the Faraday rotation of geostationary satellite signals. Planet Space Sci 20(3):353–369. https://doi.org/10.1016/0032-0633(72)90034-7

Titheridge JE (1973) The slab thickness of the mid-latitude ionosphere. Planet Space Sci 21(10):1775–1793. https://doi.org/10.1016/0032-0633(73)90168-2

Tyagi TR, Somayajulu YV (1966) Some results of electron content measurements at Delhi from faraday fading of S-66 transmissions. Radio Sci 1:1125. https://doi.org/10.1002/rds19661101125

Wright JW (1960) A model of the F region above h_{max}F2. J Geophys Res 65(1):185–191. https://doi.org/10.1029/JZ065i001p00185

Zolesi B, Cander L (2014) Ionospheric prediction and forecasting. Springer, Berlin. https://doi.org/10.1007/978-3-642-38430-1